Final Draft
of the original manuscript:

Jia, G.; Chen, C.; Zhang, J.; Wang, Y.; Yue, R.; Luthringer-Feyerabend, B.J.C.; Willumeit-Roemer, R.; Zhang, H.; Xiong, M.; Huang, H.; Yuan, G.; Feyerabend, F.:

In vitro degradation behavior of Mg scaffolds with three-dimensional interconnected porous structures for bone tissue engineering.

In: Corrosion Science. Vol. 144 (2018) 301 - 312.
First published online by Elsevier: 10.09.2018

DOI: /10.1016/j.corsci.2018.09.001
https://dx.doi.org/10.1016/j.corsci.2018.09.001

In vitro degradation behavior of Mg scaffolds with three-dimensional interconnected porous structures for bone tissue engineering

Gaozhi Jia[1,♣], Chenxin Chen[1,♣], Jian Zhang[1], Yinchuan Wang[1], Rui Yue[1], Bérengère J.C. Luthringer - Feyerabend[3], Regine Willumeit-Roemer[3], Hua Zhang[1], Meiping Xiong[2,*], Hua Huang[1,*], Guangyin Yuan[1,*] Frank Feyerabend[3,*]

[1]National Engineering Research Center of Light Alloy Net Forming and State Key Laboratory of Metal Matrix Composite, School of Materials Science and Engineering, Shanghai Jiao Tong University, 200240 Shanghai, P.R. China

[2]Department of Stomatology, The Fifth People's Hospital of Shanghai, Fudan University, Shanghai, 200240, P.R. China

[3]Institute of Materials Research, Division Metallic Biomaterials, Helmholtz-Zentrum Geesthacht, Max-Planck-Str.1, 21502 Geesthacht, Germany

♣ Authors equally contributed to this work.

*Corresponding authors.

E-mail addresses: gyyuan@sjtu.edu.cn (G. Yuan), xmpygy@163.com (M. Xiong), huangh@sjtu.edu.cn (H. Huang), frank.feyerabend@hzg.de (F. Feyerabend)

Abstract

The degradation behavior in consideration of the pore strut and the interconnectivity of two Mg scaffolds with different three-dimensional interconnected porous structures were evaluated. The interconnectivity of the two scaffolds gradually decreased along with the clogged interconnected

pores due to the deposition formation on the pore wall. Mg scaffold with spherical pores and cambered pore strut degraded faster but exhibited better resistance to the deterioration of the interconnectivity compared with Mg scaffold with irregular pores and polygonal pore struts. Direct cell culture of MC3T3-E1 osteoblasts on the two scaffolds indicated a promising potential for bone tissue engineering.

Keywords: Magnesium scaffolds; Three-dimensional; Interconnectivity; Pore strut; Degradation behavior.

1. Introduction

Bone tissue engineering scaffolds provide a promising strategy to the regeneration of segmental bone defects [1]. To achieve good therapeutic effect, the scaffold should have an open porous structure for tissue ingrowth and the exchange of nutrients and oxygen [2]. To allow a complete replacement by the regenerated host tissue, the scaffold should be degradable without leaving toxic products. Moreover, the degradation rate of tissue engineering scaffold should match the regeneration rate of new tissue [3, 4]. Mg has been intensively studied as a favorable biomaterial due to its unique degradability and comparable mechanical properties to bone tissue [5-8]. In addition, the degradation product of Mg implants can be absorbed or excreted with no harm to the host [9]. Recent studies further indicated that Mg^{2+} could stimulate the bone healing process [10], which makes Mg attractive candidate for bone tissue engineering scaffold. Meaningful progress has been acquired in designing and processing Mg scaffolds, and various porous structures of Mg scaffolds were reported [11, 12]. Mg scaffolds with square pores were fabricated by hot press sintering of pure Mg ribbons [13]. Spherical pores and irregular polyhedral pores were separately achieved by changing the space

holder particles during infiltration casting or powder metallurgy process [14-16]. Pipe-like porous structures fabricated by replicating entangled wire structures was reported with controlled pore size and porosity [17]. Topologically ordered porous WE43 magnesium alloy scaffolds have been successfully achieved by additive manufacturing [18]. However, these studies are mainly focused on Mg scaffold fabrication methods and the relationship between porous structures and mechanical properties. In fact, the porous structure not only decreases the mechanical properties [19], but also accelerate the degradation rate due to the enlarged surface area by pores [20].

To date, a few studies have been carried out to evaluate the degradation mechanism of Mg scaffolds which might largely depend on the pore characteristics including porosity, pore size, and pore strut architecture [21, 22]. Porous Mg obtained by drilling holes through bulk form showed increased mass loss with increasing porosity [23, 24]. Pipe-like Mg scaffolds with similar porosity but different pore size exhibited non-differential degradation rates [25]. Nevertheless, current studies on the degradation behavior of Mg scaffolds are primarily focused on the effect of porosity on the degradation rates [23-26]. The structural degradability in consideration of the strut architecture and the interconnectivity of Mg scaffolds has been rarely reported. Pore strut is the unit of scaffold which determines the typical performance of the porous structure [22]. The pore struts degradation behavior of Mg scaffolds could be varied due to the diverse strut architectures. Additionally, the interconnectivity of bone tissue engineering scaffold is critical in modulating the spatial transportation and the communication of biological tissues [27-29]. Therefore, the evolution of the interconnectivity of Mg scaffolds during degradation process also needs to be evaluated. Understanding the pore strut degradation behavior correlated with the interconnectivity of Mg scaffolds would be beneficial for the optimization of bone tissue engineering scaffold design and the

regulation of *in vivo* regeneration process.

In this study, two Mg scaffolds with different three-dimensional interconnected porous structures were investigated. The pore struts degradation behavior together with the interconnectivity in the form of interconnected pores of the two scaffolds were comprehensively evaluated. Cell culuture on the two Mg scaffolds was also performed in the context of the severe degradation in the porous structures.

2. Materials and methods

2.1. Preparation of Mg scaffolds

Mg scaffolds with spherical pores (denoted as S-scaffold) and Mg scaffolds with irregular polyhedral pores (denoted as I-scaffold) were separately prepared by template replication technique. The fabrication details of the two types of Mg scaffolds were reported in Ref [30]. Briefly, spherical NaCl particles and irregular polyhedral NaCl particles (China National Salt Industry Corporation, China) were, respectively, sintered in an electric resistance furnace at 720 ℃ for 24 hours to achieve open porous NaCl template, which was followed by infiltration casting process under a pressure of 0.2 MPa to fill the template with molten Mg. After solidification, a green compact of Mg and NaCl was successfully synthesized. Mg scaffolds were obtained by leaching out the NaCl template with flowing water. The scaffolds were further etched by 1 vol.% nitric acid alcohol solution in ultrasonic cleaner for 30 s to receive a clean surface. Fig. 1 shows the optical image of the two scaffolds. The actual volume of Mg scaffold was measured by Archimedean method, then the porosity was derived from the volume ratio of the pore space to the apparent volume of the scaffold. The surface area of the two Mg scaffolds was computed by software Mimics (Mimics Research 19.0.lnk, Materialise Co,

Ltd, Belgium). The pore characteristics of the two scaffolds are shown in Table 1. Disk-like specimens with a diameter of 10 mm and a thickness of 2 mm were used for the tests. Bulk Mg with the same purity as the two scaffolds (purity ≥ 99.95 wt.%, Henan Yuhang Metal Materials Co., Ltd, China) was also employed as a test group. All specimens were sterilized ultrasonically in 70 vol.% ethanol for 20 minutes, and then dried in clean bench for 2 hours before immersion tests.

2.2. Immersion tests

Semi-static immersion tests were performed in a humid environment in a standard cell incubator at 37°C with 5 vol.% CO_2. Considering the recommendation of 0.2 g/mL specimen-to-weight extraction ration given by EN IS0 10993-5 and 10993-12 is insufficient to submerge the lightweight Mg scaffolds [31]. All specimens were separately immersed in 3 mL of Dulbecco's modified eagle medium (DMEM; Gibco) supplemented with 10 vol.% fetal bovine serum (FBS; Gibco), 100 units/mL penicillin (Gibco), and 100 units/mL streptomycin (Gibco). A blank control group was also carried out by using the same amount of the medium without specimen. The medium was refreshed every 2 or 3 days, and the extracts were filtered and collected. Specimens were harvested at 7, 14, 28, 42 and 56 days, respectively.

2.3. Extract analysis

Mg^{2+} and Ca^{2+} concentrations of the extracts were determined by inductively coupled plasma optical emission spectrometer (ICP-OES; iCAP6300, Thermo, USA). The pH of the extracts was monitored with a pH meter (B-712, Horiba, Japan). The osmolality of the extracts was measured by freezing point osmometer (Osmomat 3000, Gonotec, Germany). The initial pH and osmolality of the prepared medium was 7.6 and 0.332 Osmol/kg, respectively. The increase in pH and osmolality of the extracts were derived from the corresponding results of the blank control group.

111 2.4. Scaffolds characterization after immersion tests

112 The scaffolds were evaluated by micro-computed tomography (μ-CT; Bruker Skyscan 1176, USA)
113 and scanning electron microscope (SEM; JSM 7600F, Japan) equipped with energy dispersive X-ray
114 spectroscopy (EDS). The spatial resolution of μ-CT was 9 μm. The pore size distribution of the two
115 Mg scaffolds was computed by software Mimics (Mimics Research 19.0.lnk, Materialise Co, Ltd,
116 Belgium) from μ-CT results. The diameter of maximum inscribed sphere of the pore space was
117 defined as the pore size. The pore size distribution was illustrated in column graph and linear graph
118 to show the relative quantity and the main peaks, respectively. The degradation products of the
119 specimens degraded for 56 days were collected and characterized using X-ray diffractometer (XRD;
120 Smart Lab, Japan).

121 2.5. Evaluation of the degradation rates

122 The degradation products were removed by chromic acid solution (200 g/L CrO_3 and 10 g/L $AgNO_3$
123 in distilled water, Sinopharm Chemical Reagent Co., Ltd, China). Then, the volume of the degraded
124 specimens was measured by Archimedean method. The volume loss ratio was calculated from the
125 lost volume and the volume before immersion tests. The average degradation rate in the unit of
126 mm/year was obtained using Eq. (1) [32]:

127 $$P_m = 3.65(W_{bef} - W_{aft}) / At\rho \quad (1)$$

128 Where W_{bef} is the weight of specimens before immersion tests, W_{aft} is the weight of specimens after
129 immersion tests but with no degradation products. A is the total surface area of the specimen in cm^2, t
130 is the immersion time in days, ρ is the density of pure Mg ($1.74 g/cm^3$).

131 2.6. Cell culture on Mg scaffolds

132 Osteoblastic cell line MC3T3-E1 (Cell Bank, Chinese Academy of Sciences) were cultured in

133 growth medium consisting of alpha-modified eagle's medium (α-MEM; Gibco) supplemented with
134 10 vol.% fetal bovine serum (FBS; Gibco) and 1% penicillin & streptomycin in a cell incubator at
135 humidified atmosphere with 5% CO_2 at 37 °C, with fresh medium replaced every 2 days. Mg
136 scaffolds incubated for 7 days with Dulbecco's modified eagle medium (DMEM) + 10 vol.% FBS
137 were used to conduct *in vitro* cell culture tests. Specimens were dropwise seeded with 1×10^5
138 MC3T3-E1 cells, and then placed in 12-well plates with 3 mL of the cell culture medium, the
139 medium was refreshed every 24 hours. After incubation for 6 hours, 24 hours and 72 hours on Mg
140 scaffolds, the supernatants were collected, and the cells were gently rinsed with Dulbecco phosphate
141 buffered saline (DPBS; HyClone), and then placed in 24-well plate. For cell viability and
142 proliferation assay, 0.5 mL of the cell culture medium and 50 μL of Cell Counting Kit-8 (CCK8
143 solution; Beyotime Biological Technology Co., Ltd, China) were added to the 24-well plate and
144 incubated in a cell incubator for 2 hours, then the extracts were measured by the optical density (OD)
145 measurement at 450 nm with a microplate reader (imark, Bio-Rad, USA). For direct cell adhesion
146 assay, the cells were stained with Calcein-AM and Ethidium homodimer-1 reagents (LIVE/DEAD
147 Viability/Cytotoxicity Assay Kit, Thermo Fisher Scientific Inc, USA) for 15 min at 37 °C. After
148 gently rinsing twice with DPBS, samples were mounted in 24-well plate for fluorescence microscopy
149 observation (IX71, Olympus, Japan). For lactate dehydrogenase assay (LDH; Beyotime Biological
150 Technology Co., Ltd, China), the supernatant was tested according to the protocol from the
151 manufacturer. Specimens without cells were used as blank control group. Cell culture on the bulk
152 Mg incubated for 7 days was not showed here because the dense MC3T3-E1 cells resulted in
153 indistinctive results of Live-Dead staining within 72 hours, and the cell quantity on the specimen was
154 not comparabe with the scaffold groups due to the buk form.

155 2.7. Statistics and data analysis

156 The results were expressed as the mean ± standard deviations. All the tests were conducted in
157 triplicates for each group at each time and repeated three times. SPSS statistics 19 for Windows, one-
158 way ANOVA with Dunn's multiple comparison post hoc tests were used to analyze the data. $p <$
159 0.05 was considered statistically significant.

160 ## 3. Results

161 3.1. Evaluation of the extracts

162 The degradation effects of Mg scaffolds on the corrosive medium were evaluated through the change
163 of Mg^{2+} concentration, Ca^{2+} concentration, pH and osmolality, as shown in Fig. 2. Fig. 2a and b
164 show the short-term and long-term variation of Mg^{2+} concentration in the extracts, respectively. The
165 Mg^{2+} concentration of the three groups increased rapidly from about 20 ppm to over 100 ppm after 6
166 h, then the concentration was doubled after another 6 h. The scaffolds groups showed significantly
167 higher Mg^{2+} concentration than the bulk group after 6 h and 12 h. The Mg^{2+} concentration of all three
168 groups increased to over 1000 ppm after immersion for 3 d. At 14 d the Mg^{2+} concentration of the
169 two scaffolds groups was remarkably decreased to lower than 850 ppm. However, I-scaffold group
170 exhibited much higher Mg^{2+} concentration than S-scaffold group during the immersion tests. The
171 short-term and long-term change of Ca^{2+} concentration are shown in Fig. 2c and d, respectively. The
172 Ca^{2+} concentration of the three groups largely dropped after immersion for 6 h, while the two
173 scaffold groups exhibited lower Ca^{2+} concentration than the bulk group. I-scaffold group showed a
174 significant lower Ca^{2+} concentration than S-scaffold group at 6 h and 12 h. The Ca^{2+} concentration of
175 the three groups started to increase after 3 d and became stable at 14 d, during which the Ca^{2+}
176 concentration of I-scaffold group was lower than S-scaffold group. After 56 d, the Ca^{2+}

concentrations of all three groups were still lower than that of the initial value of the medium, which indicated the continuous deposition of Ca^{2+}. Fig. 2e shows that the pH of the three groups largely increased compared to the control group. A peak of the increment was observed at 12 h for the scaffolds groups, and I-scaffold group showed a higher increment of pH than S-scaffold group. The increasing tendency of pH in the tested groups decreased slowly after 3 d, as shown in Fig. 2f. Fig. 2g and h show significant increase in the osmolality of the extracts after immersion for 3 d, and the increment was stabilized after 14 d. The trend of the increase in osmolality was similar for the three groups, while the bulk group showed a higher change after 3 d. Collectively, the three-dimensional interconnected porous structures showed more apparent influence on the change of the medium condition than the bulk material.

3.2. Surface morphology of the degraded Mg scaffolds

The optical appearance of the representative degraded specimens is displayed in Fig. 3. Visible degradation products were found on the surface of the two Mg scaffolds at 7 d, but the pores were still recognizable for both scaffolds. After immersion for 14 d, more degradation products can be found on the surface of the three groups, and the degradation layer was thicker after 56 d. The magnified surface morphology of the representative degraded scaffolds are shown in Fig. 4. Fig. 4a and b show the initial porous structures of S-scaffold and I-scaffold, which consist of the main pores (dashed lines) and the interconnected pores (arrows), respectively. Fig. 4c shows that a degradation layer is found on the pore wall of S-scaffold after 7 d, but the main pores and most of the interconnected pores are visible. Fig. 4d indicates a similar degradation layer in I-scaffold, but fewer interconnected pores are recognizable. The degradation layer of the two scaffolds at 7 d is mainly composed of sheet-like degradation products, as shown in the inserted images with magnified view

in Fig. 4c and d. After immersion for 14 d, the surface sheet-like degradation products were replaced by rod-like degradation products, as shown in the inserted images in Fig. 4e and f. In addition, the surface main pores of the two scaffolds were nearly half filled with the rod-like degradation products (Fig. 4e and f), which simultaneously clogged the surface interconnected pores. After 56 d the surface pores of both scaffolds were filled with the rod-like degradation products, as shown in Fig. 4g and h. EDS analysis in Fig. 4i and j implied that the degradation products of both scaffolds were similar and mainly composed of Mg, O, Ca, P, C, Na, Cl and N. Collectively, the surface deposition of the two scaffolds became thicker and denser with the increasing immersion time, which gradually filled the surface pores.

3.3. XRD analysis of the degradation products

To further confirm the phase composition of the deposited substances XRD analysis was applied to the degradation products of the degraded specimens at 56 d, as shown in Fig. 5. The composition of the degradation products was similar for the three groups. In addition to the diffraction peaks for Mg, the other peaks can be identified as $MgCO_3 \cdot 3H_2O$, calcium phosphate salts and $Mg(OH)_2$. The XRD results implied that the degradation products of the two Mg scaffolds were independent of the two porous structures.

3.4. μ-CT analysis of the degraded Mg scaffolds

μ-CT was employed to observe the cross-sectional distribution of the degradation products. Fig. 6 shows the microstructures of the representative degraded scaffolds. After immersion for 14 d, different contrast near the pore wall can be observed, as shown in Fig. 6b. The bright part represented Mg substrate while the grey part represented the degradation products due to different densities [33]. The thickness of the degradation products on the surface of S-scaffold increased after

28 d, as shown in Fig. 6c. Fig. 6d indicates that the thickness of S-scaffold substrate largely decreased at 56 d compared to the result in Fig. 6a. The same change of the surface degradation layer and the decrease in substrate thickness was also found for I-scaffold, as shown in Fig. 6f, g and h. Despite the external pores of the two scaffolds were filled with degradation products at 56 d, the internal structures of the two scaffolds were still porous during the immersion tests. Additionally, the thickness of the degradation layer on the internal pore wall barely increased during the immersion tests. Thus, different degradation rates between the external porous structure and the internal porous structure were revealed in the two Mg scaffolds.

3.5. Surface observation of the scaffolds after removal of degradation products

The visual appearance of the representative specimens after the removal of degradation products is shown Fig. 7a. The open porous structures and visible volume decreased with the increase of immersion time were observed for the two scaffold groups. S-scaffold displayed more objective volume decrease in diameter at 56 d compared to I-scaffold. Fig. 7b and c show that the pore morphologies of the two scaffolds are retained and still consist of main pores and interconnected pores after 56 d. However, the size of the interconnected pores was enlarged due to the degradation of pore struts, as marked by the dashed lines in Fig. 7b on the extended edge of the pores. Because of the random size distribution and the complex morphologies of the initial interconnected pores in I-scaffold, the enlarged interconnected pores could hardly be identified. The inserted images in Fig. 7b and c indicate that the pore wall of both scaffolds experienced severe pitting corrosion. Therefore, the size of main pores in the two Mg scaffolds may also be extended.

3.6. Pore size distribution

The pore size distribution of the two Mg scaffolds after the removal of degradation products

exhibited the similar double peaks as the initial porous structures which represented the distribution of the main pores and the interconnected pores, respectively, as shown in Fig. 8. However, the degraded Mg scaffolds exhibited decreased pore quantity with the increase of immersion time. In addition, a shift of the predominated peeks to larger pore size was observed from the fitted curves, as shown in Fig. 8b and d. The pore size distribution indicated that the main pores and the interconnected pores of the two Mg scaffolds were enlarged during the degradation process.

3.7. Degradation rates of Mg scaffolds

Fig. 9a displays that S-scaffold lost about 30 vol.% when I-scaffold lost about 40 vol.% at 7 d. After 56 d S-scaffold lost about 70 vol.%, I-scaffold lost about 60 vol.%. The average degradation rates of the two scaffolds are shown in Fig. 9b. The degradation rates of S-scaffold were 4.36 ± 0.37 mm/y at 7 d and 1.34 ± 0.04 mm/y at 56 d, while I-scaffold exhibited a degradation rate of 2.83 ± 0.11mm/y at 7 d and 0.52 ± 0.01 mm/y at 56 d. The penetration degradation rates for the bulk group at 7 d was 0.93 ± 0.07 mm/y and 0.44 ± 0.02 mm/y at 56 d. S-scaffold exhibited faster degradation rates than I-scaffold during the whole tests in spite of the significant decrement with the increase of immersion time.

3.8. Cell culture in Mg scaffolds

Although the same quantity of MC3T3-E1 osteoblasts were dropwise seeded on the two Mg scaffolds, the number of actual adhered cells on S-scaffold and I-scaffold were different and much less than the expected amount due to the porosities and the surface area. Fig. 10a and b show the live-dead staining results of S-scaffold after incubating for 6 h and 24 h, respectively. After 24 h, a decrease of cell number in S-scaffolds was observed in Fig. 10b. After incubation for 72 h, adhered cells spread out in S-scaffolds, as shown in Fig. 10c. Only a few dead cells were found in the porous

structures after the staining while most of the dead cells might be rinsed into underlying pores. The similar live-dead staining results were also found in I-scaffold, as shown in Fig. 10d, e and f, but more cells were observed on I-scaffolds at 6 h. Cell viability results in Fig. 10g reveals that I-scaffold was loaded with more cells than S-scaffold due to the higher specific surface area. However, according to the evaluation of the extracts in immersion tests the medium condition influenced by the degradation of I-scaffold was more severe due to the larger surface area. Therefore, a sharp reduction in cell viability was found for I-scaffold group at 24 h. Then, an increment of cell viability was observed at 72 h for the two scaffolds. The LDH activity results in Fig. 10h indicates that more cells are necrotic in I-scaffold and the number increased with incubation time.

4. Discussion

Mg is easy to be constantly degraded in the corrosive medium due to its chemical activity with H_2O and the aggressive attack of Cl^- according to Eq. (2) and Eq. (3) [34-36].

$$Mg\,(s) + 2H_2O\,(l) \rightarrow Mg(OH)_2\,(s) + H_2\,(g) \quad (2)$$

$$Mg(OH)_2\,(s) + 2Cl^- \rightarrow Mg^{2+} + 2Cl^- + 2OH^- \quad (3)$$

The two Mg scaffolds possessed larger surface area than the bulk form due to the porous structures, and the interconnected pores provided multidirectional channels to contact the DMEM medium. Therefore, a sharp increase in Mg^{2+} concentration was observed in the extracts within 3 d, as shown in Fig. 2a and b. The fast release of Mg^{2+} in the medium caused an abrupt increase in osmolality shown in Fig. 2g. The degradation of two Mg scaffolds simultaneously caused an alkaline environment revealed in Fig. 2e, f and Eq. (3). With the abundant amount of HCO_3^- in the DMEM

medium, the alkaline environment could benefit the formation of $MgCO_3 \cdot 3H_2O$ in the degradation products according to Eq. (4) and Eq. (5) [37]:

$$HCO_3^- + OH^- \rightarrow CO_3^{2-} + H_2O\ (l) \quad (4)$$

$$Mg^{2+} + CO_3^{2-} \rightarrow MgCO_3\ (s) \quad (5)$$

Meanwhile, the alkaline environment might also facilitate the deposition of calcium phosphate salts on Mg surface [38, 39]. The sharp decrease of Ca^{2+} concentration showed in Fig. 2c and d provided the evidence of calcium deposition. Due to the higher specific surface area shown in Table 1, I-scaffold exposed more surface area to the corrosive medium than S-scaffold. Thus, the change of Mg^{2+} concentration and Ca^{2+} concentration for I-scaffold group were larger. It is worth noting that refreshing the DMEM medium could constantly supply HCO_3^-, Ca^{2+} and phosphate, which would accelerate the deposition of the degradation products. The deposition products could inhibit the degradation of Mg substrate as a protective coating [40-42]. Therefore, the effect of the degradation on the environmental change of the corrosive medium decreased after 3 d. Moreover, after 14 d the surface interconnected pores of both scaffolds were clogged by the rod-like degradation products, which could dramatically decrease the exposed surface area. Consequently, the protecting effect of the degradation layer could be further enhanced.

Besides the inorganic mineral participating in the deposition, the supply of proteins in the 10 vol.% FBS may also be involved in the degradation layer [43]. It has been reported that proteins could lead to a thicker but less dense degradation layer on degraded Mg substrate [44], which could contribute to the increased thickness of the external degradation layer after 28 d. However, the degradation layer of inner porous structures of the two Mg scaffolds was insensitive to the immersion time.

306 Although the internal degradation process might still proceed by the penetration of the aqueous
307 medium [44], the supply of the DMEM medium could be effectively filtered due to the barrier effect
308 generated by the clogged external pores and the degradation layer. Thus, the increase in the thickness
309 of the internal degradation layer was unapparent. An illustration of the initial degradation and the
310 deposition formation process of the two three-dimensional interconnected porous structures is shown
311 in Fig. 11a-d. The porous structures of the two Mg scaffolds exhibited similar degradation behavior
312 at the initial stage, i.e. magnesium substrate degradation and depositon formation, as shown in Fig.
313 11a and b. However, the rapidly released Mg^{2+} through the three-dimensional porous structure into
314 the extract and the constant alkaline environment could accelerate the formation of the deposition,
315 which would gradually decrease the interconnectivity of the porous structures, as shown in Fig. 11c
316 and d. In addition, the interconnected pores of I-scaffold were more likely to be clogged by the
317 deposition due to the existence of smaller interconnected pores in the range of 0-150 μm compared to
318 S-scaffold.

319 The interconnectivity, i.e. the interconnected pore of tissue engineering scaffolds is crucial for the
320 survivability of progenitor cells, as well as maintaining the exchange of nutrients and oxygen [22, 45,
321 46]. The minimum size for interconnected pore to enable the exchange of metabolic components and
322 to facilitate cell entrance is proposed to be 30 to 40 μm [47, 48]. S-scaffold with interconnected pore
323 size in the range of 150-400 μm displayed better interconnectivity than I-scaffold with
324 interconnected pore size in the range of 0-400 μm, whereby S-scaffold exhibited better resistance to
325 the deterioration of the interconnectivity within 7 d. However, the external interconnected pores of S-
326 scaffold were also entirely clogged by the deposition in surface pores after 14 d. Since then, the
327 interconnectivity of the two Mg scaffolds would be greatly decreased and resulted in the isolation of

328 the internal porous structure. As the interface between bone and scaffold is critical to the successful
329 clinical applications [49], the fast deposition process of Mg scaffolds could obstruct the tissue
330 ingrowth and give rise to poor osseointegration [50]. Fortunately, the deposition rate could be
331 decreased *in vivo* on account of the much slower degradation rates of Mg-based implants [51-53].
332 Furthermore, the dynamic body fluid could constantly reduce the local Mg^{2+} concentration and
333 remove the degradation products when passing through the pores [54, 55]. Therefore, the
334 interconnectivity of the two Mg scaffolds could be maintained when tissue environments are
335 involved. Recent development of coating technologies on Mg substrates could further enhance the
336 degradation resistance to reduce the deposition rate [56, 57]. Besides, the two scaffolds displayed
337 enlarged interconnected pores and main pores after degraded for 28 d and 56 d, which implied that
338 the degradation might benefit the interconnectivity by enlarging the pore size at a controlled
339 degradation rate.

340 The degradation process of the two Mg scaffolds displayed a volume decrease from the external pore
341 struts to the internal pore struts in thickness and diameter directions (Fig. 6d, Fig. 6h and Fig. 7a).
342 Thus, the two three-dimensional interconnected porous structures exhibited the same degradation
343 mode. The reason could be related to the similar deposition mechanism, i.e. different deposition rates
344 between the external and internal pore struts. After the external pore struts were converted into
345 degradation products, new exposed pore struts would be similarly clogged. Therefore, the observed
346 volume decrease mode was exhibited in present study. However, S-scaffold exhibited faster
347 degradation rates during the whole immersion tests and higher volume loss ratio after 28 d compared
348 with I-scaffold. The different volume loss ratio and degradation rates between the two scaffolds
349 could be related to the architecture of the pore strut. The pore strut degradation mechanism of the

two scaffolds was depicted in Fig.11e and f, respectively. The strut thickness of S-scaffold and I-scaffold displayed similar smooth decrease towards the edge of interconnected pores. Nevertheless, the cambered pore struts in S-scaffold could cause sectional struts thinner comparing with the polygonal pore struts in I-scaffold, which might result in poor degradation resistance. Thus, the earlier strut loss due to the connection break at the thinner parts in S-scaffold would contribute to faster volume decrease as well as higher degradation rates, while I-scaffold could possess better structural integrity with thicker pore strut.

Direct *in vitro* cell incubation could hardly succeed on the untreated Mg scaffolds because of the initial severe medium condition in pores indicated by the immersion tests. As mentioned above, the degradation of the Mg scaffolds might be greatly retarded *in vivo*. Therefore, cell seeding on the pre-incubated Mg scaffolds with protective deposition layer could be reasonably performed. Moreover, three-dimensional cell culture *in vitro* could simulate the previous biological tissue response to the porous structure of tissue engineering scaffold [58]. We tended to evaluate the relationship between the three-dimensional porous structures and the cell adhesion behaviour. Although the cell culture results revealed that the two three-dimensional interconnected porous structures might be promising bone tissue engineering scaffolds, the severe medium condition due to the fast degradation of Mg substrate and the varying degradation rates directly inhibited the cell viability as well as the proliferation behaviour. To further investigate the cell behavior in the two Mg scaffolds, bioactive coating is required to be developed on the pore strut to achieve moderate degradation rates. Besides, cell culture on the scaffolds could be conducted within a bioreactor to simulate the dynamic physiological environment [59]. The circulation of cell culture medium could also consistently support the metabolism of the seeded cells avoiding the supply shortage in the internal porous

structures in consideration of the barrier effect inherited from the pores. Further *in vivo* studies are needed to investigate the effect of different pore struts on the regeneration ability.

5. Conclusions

We comprehensively studied the degradation behavior of two Mg scaffolds with different three-dimensional interconnected porous structures. The external porous structures of the two scaffolds were gradually filled with the degradation products, which resulted in decreased interconnectivity and different degradation rates between the external and internal porous structures. However, the three-dimensional interconnected porous structures of Mg substrate were retained in the experimental period of 56 d. S-scaffold with uniform porous structure and larger interconnected pores exhibited better resistance to the deterioration of the interconnectivity. Together with the *in vitro* cell culture assay, our results could bring insights into the pore strut degradation behavior and the evolution of the interconnectivity of biodegradable bone tissue engineering scaffolds.

Authors' contributions

Conceived and designed the study: HH, FF and GYY. Performed the experiments: GZJ and CXC. Contributed regents/materials/analysis tools: JZ, YCW, RY, MPX and HZ. Analysed and discussed the data: GZJ, CXC, FF, HH, MPX and GYY. Wrote the paper: GZJ. Review and edited the manuscript: HH, FF, BL, RW, MPX and GYY. All authors read and approved the manuscript.

Conflicts of interest

The authors declare no conflict of interest.

Data availability

The raw/processed data required to reproduce these findings cannot be shared at this time as the data also forms part of an ongoing study.

Acknowledgement

This work was supported by the National Natural Science Foundation of China (No. 51571143), the National Key Research and Development Program of China (No. 2016YFC1102103), the Science and Technology Commission of Shanghai Municipality (No. 18441908000, 17440730700 and 17XD1402100) and Shanghai Municipal Commission of Health and Family Planning (201640281).

References

[1] A.R. Shrivats, M.C. McDermott, J.O. Hollinger, Bone tissue engineering: state of the union, Drug Discovery Today 19(6) (2014) 781-786.

[2] S. Gomez, M.D. Vlad, J. Lopez, E. Fernandez, Design and properties of 3D scaffolds for bone tissue engineering, Acta Biomater 42 (2016) 341-50.

[3] X. Guan, M. Xiong, F. Zeng, B. Xu, L. Yang, H. Guo, J. Niu, J. Zhang, C. Chen, J. Pei, H. Huang, G. Yuan, Enhancement of osteogenesis and biodegradation control by brushite coating on Mg-Nd-Zn-Zr alloy for mandibular bone repair, ACS Appl Mater Interfaces 6(23) (2014) 21525-33.

[4] A.H. Yusop, A.A. Bakir, N.A. Shaharom, M.R. Abdul Kadir, H. Hermawan, Porous biodegradable metals for hard tissue scaffolds: a review, Int J Biomater 2012 (2012) 641430.

[5] Y. Yun, Z. Dong, N. Lee, Y. Liu, D. Xue, X. Guo, J. Kuhlmann, A. Doepke, H.B. Halsall, W. Heineman, Revolutionizing biodegradable metals, Mater. Today 12(10) (2009) 22-32.

[6] M. Esmaily, J.E. Svensson, S. Fajardo, N. Birbilis, G.S. Frankel, S. Virtanen, R. Arrabal, S. Thomas, L.G. Johansson, Fundamentals and advances in magnesium alloy corrosion, Prog. Mater Sci. 89 (2017) 92-193.

[7] X.J. Wang, D.K. Xu, R.Z. Wu, X.B. Chen, Q.M. Peng, L. Jin, Y.C. Xin, Z.Q. Zhang, Y. Liu, X.H. Chen, G. Chen, K.K. Deng, H.Y. Wang, What is going on in magnesium alloys?, Journal of Materials Science & Technology 34(2) (2018) 245-247.

[8] R.-C. Zeng, L. Sun, Y.-F. Zheng, H.-Z. Cui, E.-H. Han, Corrosion and characterisation of dual phase Mg–Li–Ca alloy in Hank's solution: The influence of microstructural features, Corros. Sci. 79 (2014) 69-82.

[9] D. Zhao, F. Witte, F. Lu, J. Wang, J. Li, L. Qin, Current status on clinical applications of magnesium-based orthopaedic implants: A review from clinical translational perspective, Biomaterials 112 (2017) 287-302.

[10] Y. Zhang, J. Xu, Y.C. Ruan, M.K. Yu, M. O'Laughlin, H. Wise, D. Chen, L. Tian, D. Shi, J. Wang, S. Chen, J.Q. Feng, D.H. Chow, X. Xie, L. Zheng, L. Huang, S. Huang, K. Leung, N. Lu, L. Zhao, H. Li, D. Zhao, X. Guo, K. Chan, F. Witte, H.C. Chan, Y. Zheng, L. Qin, Implant-derived magnesium induces local neuronal production of CGRP to improve bone-fracture healing in rats, Nat Med 22(10) (2016) 1160-1169.

[11] K. Bobe, E. Willbold, I. Morgenthal, O. Andersen, T. Studnitzky, J. Nellesen, W. Tillmann, C. Vogt, K. Vano, F. Witte, In vitro and in vivo evaluation of biodegradable, open-porous scaffolds made of sintered magnesium W4 short fibres, Acta Biomater 9(10) (2013) 8611-23.

[12] J.O. Osorio-Hernández, M.A. Suarez, R. Goodall, G.A. Lara-Rodriguez, I. Alfonso, I.A. Figueroa, Manufacturing of

428 open-cell Mg foams by replication process and mechanical properties, Mater. Des. 64 (2014) 136-141.
429 [13] X. Zhang, X.W. Li, J.G. Li, X.D. Sun, Preparation and mechanical property of a novel 3D porous magnesium
430 scaffold for bone tissue engineering, Mater Sci Eng C Mater Biol Appl 42 (2014) 362-7.
431 [14] G. Jia, Y. Hou, C. Chen, J. Niu, H. Zhang, H. Huang, M. Xiong, G. Yuan, Precise fabrication of open porous Mg
432 scaffolds using NaCl templates: Relationship between space holder particles, pore characteristics and mechanical
433 behavior, Mater. Des. 140 (2018) 106-113.
434 [15] G.L. Hao, F.S. Han, W.D. Li, Processing and mechanical properties of magnesium foams, J. Porous Mater. 16(3)
435 (2008) 251-256.
436 [16] J. Trinidad, I. Marco, G. Arruebarrena, J. Wendt, D. Letzig, E. Sáenz de Argandoña, R. Goodall, Processing of
437 Magnesium Porous Structures by Infiltration Casting for Biomedical Applications, Adv. Eng. Mater. 16(2) (2014) 241-
438 247.
439 [17] G. Jiang, G. He, A new approach to the fabrication of porous magnesium with well-controlled 3D pore structure for
440 orthopedic applications, Mater Sci Eng C Mater Biol Appl 43 (2014) 317-20.
441 [18] Y. Li, J. Zhou, P. Pavanram, M.A. Leeflang, L.I. Fockaert, B. Pouran, N. Tümer, K.U. Schröder, M. Jmc, H.
442 Weinans, Additively manufactured biodegradable porous magnesium, Acta Biomater (2018) 378-392.
443 [19] L. Tan, M. Gong, F. Zheng, B. Zhang, K. Yang, Study on compression behavior of porous magnesium used as bone
444 tissue engineering scaffolds, Biomed Mater 4(1) (2009) 015016.
445 [20] E. Aghion, Y. Perez, Effects of porosity on corrosion resistance of Mg alloy foam produced by powder metallurgy
446 technology, Mater. Charact. 96 (2014) 78-83.
447 [21] J.A. Kim, J. Lim, R. Naren, H.S. Yun, E.K. Park, Effect of the biodegradation rate controlled by pore structures in
448 magnesium phosphate ceramic scaffolds on bone tissue regeneration in vivo, Acta Biomater 44 (2016) 155-67.
449 [22] S.J. Hollister, Porous scaffold design for tissue engineering, Nat. Mater. 4(7) (2005) 518-24.
450 [23] A.P. Md. Saad, N. Jasmawati, M.N. Harun, M.R. Abdul Kadir, H. Nur, H. Hermawan, A. Syahrom, Dynamic
451 degradation of porous magnesium under a simulated environment of human cancellous bone, Corros. Sci. 112 (2016)
452 495-506.
453 [24] A.P. Md Saad, A. Syahrom, Study of dynamic degradation behaviour of porous magnesium under physiological
454 environment of human cancellous bone, Corros. Sci. 131 (2018) 45-56.
455 [25] M.Q. Cheng, T. Wahafu, G.F. Jiang, W. Liu, Y.Q. Qiao, X.C. Peng, T. Cheng, X.L. Zhang, G. He, X.Y. Liu, A
456 novel open-porous magnesium scaffold with controllable microstructures and properties for bone regeneration, Sci Rep 6
457 (2016) 24134.
458 [26] W. Liu, J. Wang, G. Jiang, J. Guo, Q. Li, B. Li, Q. Wang, M. Cheng, G. He, X. Zhang, The improvement of
459 corrosion resistance, biocompatibility and osteogenesis of the novel porous Mg–Nd–Zn alloy, J Mater Chem B 5(36)
460 (2017).
461 [27] Y.S. Zhang, C. Zhu, Y. Xia, Inverse Opal Scaffolds and Their Biomedical Applications, Adv. Mater. 29(33) (2017).
462 [28] L. Polo-Corrales, M. Latorre-Esteves, J.E. Ramirez-Vick, Scaffold Design for Bone Regeneration, J Nanosci
463 Nanotechno 14(1) (2014) 15-56.
464 [29] Q.L. Loh, C. Choong, Three-dimensional scaffolds for tissue engineering applications: role of porosity and pore
465 size, Tissue Eng Part B Rev 19(6) (2013) 485-502.
466 [30] G. Jia, Y. Hou, C. Chen, J. Niu, H. Zhang, H. Huang, M. Xiong, G. Yuan, Precise fabrication of open porous Mg
467 scaffolds using NaCl templates: Relationship between space holder particles, pore characteristics and mechanical
468 behavior, Mater. Des. 140(Supplement C) (2018) 106-113.
469 [31] J. Wang, F. Witte, T. Xi, Y. Zheng, K. Yang, Y. Yang, D. Zhao, J. Meng, Y. Li, W. Li, Recommendation for
470 modifying current cytotoxicity testing standards for biodegradable magnesium-based materials, Acta Biomater 21 (2015)
471 237-249.

[32] M.-C. Zhao, P. Schmutz, S. Brunner, M. Liu, G.-l. Song, A. Atrens, An exploratory study of the corrosion of Mg alloys during interrupted salt spray testing, Corros. Sci. 51(6) (2009) 1277-1292.
[33] M. Syha, W. Rheinheimer, M. Bäurer, E.M. Lauridsen, W. Ludwig, D. Weygand, P. Gumbsch, Three-dimensional grain structure of sintered bulk strontium titanate from X-ray diffraction contrast tomography, Scripta Mater. 66(1) (2012) 1-4.
[34] Y. Shi, J. Pei, L. Zhang, B.K. Lee, Y. Yun, J. Zhang, Z. Li, S. Gu, K. Park, G. Yuan, Understanding the effect of magnesium degradation on drug release and anti-proliferation on smooth muscle cells for magnesium-based drug eluting stents, Corros. Sci. 123 (2017) 297-309.
[35] M. Ascencio, M. Pekguleryuz, S. Omanovic, An investigation of the corrosion mechanisms of WE43 Mg alloy in a modified simulated body fluid solution: The influence of immersion time, Corros. Sci. 87 (2014) 489-503.
[36] R. Wu, Y. Yan, G. Wang, L.E. Murr, W. Han, Z. Zhang, M. Zhang, Recent progress in magnesium–lithium alloys, Int. Mater. Rev. 60(2) (2014) 65-100.
[37] D. Tie, F. Feyerabend, N. Hort, R. Willumeit, D. Hoeche, XPS studies of magnesium surfaces after exposure to Dulbecco's modified eagle medium, Hank's buffered salt solution, and simulated body fluid, Adv. Eng. Mater. 12(12) (2010).
[38] D.M. Miskovic, K. Pohl, N. Birbilis, K.J. Laws, M. Ferry, Formation of a phosphate conversion coating on bioresorbable Mg-based metallic glasses and its effect on corrosion performance, Corros. Sci. 129(Supplement C) (2017) 214-225.
[39] A. Bigi, G. Falini, E. Foresti, A. Ripamonti, M. Gazzano, N. Roveri, Magnesium influence on hydroxyapatite crystallization, J. Inorg. Biochem. 49(1) (1993) 69-78.
[40] J. Hofstetter, E. Martinelli, A.M. Weinberg, M. Becker, B. Mingler, P.J. Uggowitzer, J.F. Löffler, Assessing the degradation performance of ultrahigh-purity magnesium in vitro and in vivo, Corros. Sci. 91 (2015) 29-36.
[41] X. Li, X. Liu, S. Wu, K.W. Yeung, Y. Zheng, P.K. Chu, Design of magnesium alloys with controllable degradation for biomedical implants: From bulk to surface, Acta Biomater 45 (2016) 2-30.
[42] G. Duan, L. Yang, S. Liao, C. Zhang, X. Lu, Y. Yang, B. Zhang, Y. Wei, T. Zhang, B. Yu, Designing for the chemical conversion coating with high corrosion resistance and low electrical contact resistance on AZ91D magnesium alloy, Corros. Sci. 135 (2018) 197-206.
[43] J. Zhang, N. Kong, Y. Shi, J. Niu, L. Mao, H. Li, M. Xiong, G. Yuan, Influence of proteins and cells on in vitro corrosion of Mg–Nd–Zn–Zr alloy, Corros. Sci. 85 (2014) 477-481.
[44] R. Willumeit, J. Fischer, F. Feyerabend, N. Hort, U. Bismayer, S. Heidrich, B. Mihailova, Chemical surface alteration of biodegradable magnesium exposed to corrosion media, Acta Biomater 7(6) (2011) 2704-2715.
[45] A.L. Butcher, G.S. Offeddu, M.L. Oyen, Nanofibrous hydrogel composites as mechanically robust tissue engineering scaffolds, Trends Biotechnol. 32(11) (2014) 564-70.
[46] L.S. Wray, K. Tsioris, E.S. Gi, F.G. Omenetto, D.L. Kaplan, Slowly degradable porous silk microfabricated scaffolds for vascularized tissue formation, Adv. Funct. Mater. 23(27) (2013) 3404-3412.
[47] L.R. Madden, D.J. Mortisen, E.M. Sussman, S.K. Dupras, J.A. Fugate, J.L. Cuy, K.D. Hauch, M.A. Laflamme, C.E. Murry, B.D. Ratner, Proangiogenic scaffolds as functional templates for cardiac tissue engineering, Proceedings of the National Academy of Sciences 107(34) (2010) 15211-15216.
[48] O. Oliviero, M. Ventre, P. Netti, Functional porous hydrogels to study angiogenesis under the effect of controlled release of vascular endothelial growth factor, Acta Biomater 8(9) (2012) 3294-3301.
[49] C. Castellani, R.A. Lindtner, P. Hausbrandt, E. Tschegg, S.E. Stanzl-Tschegg, G. Zanoni, S. Beck, A.M. Weinberg, Bone-implant interface strength and osseointegration: Biodegradable magnesium alloy versus standard titanium control, Acta Biomater 7(1) (2011) 432-40.
[50] Y. Zhao, H.M. Wong, W. Wang, P. Li, Z. Xu, E.Y.W. Chong, C.H. Yan, K.W.K. Yeung, P.K. Chu,

516 Cytocompatibility, osseointegration, and bioactivity of three-dimensional porous and nanostructured network on
517 polyetheretherketone, Biomaterials 34(37) (2013) 9264-9277.
518 [51] J. Niu, M. Xiong, X. Guan, J. Zhang, H. Huang, J. Pei, G. Yuan, The in vivo degradation and bone-implant interface
519 of Mg-Nd-Zn-Zr alloy screws: 18 months post-operation results, Corros. Sci. 113 (2016) 183-187.
520 [52] P. Han, P. Cheng, S. Zhang, C. Zhao, J. Ni, Y. Zhang, W. Zhong, P. Hou, X. Zhang, Y. Zheng, Y. Chai, In vitro and
521 in vivo studies on the degradation of high-purity Mg (99.99wt.%) screw with femoral intracondylar fractured rabbit
522 model, Biomaterials 64 (2015) 57-69.
523 [53] A.H. Martinez Sanchez, B.J. Luthringer, F. Feyerabend, R. Willumeit, Mg and Mg alloys: how comparable are in
524 vitro and in vivo corrosion rates? A review, Acta Biomater 13 (2015) 16-31.
525 [54] A.P. Md Saad, R.A. Abdul Rahim, M.N. Harun, H. Basri, J. Abdullah, M.R. Abdul Kadir, A. Syahrom, The
526 influence of flow rates on the dynamic degradation behaviour of porous magnesium under a simulated environment of
527 human cancellous bone, Mater. Des. 122 (2017) 268-279.
528 [55] T. Kokubo, H. Takadama, How useful is SBF in predicting in vivo bone bioactivity?, Biomaterials 27(15) (2006)
529 2907-15.
530 [56] J. Niu, G. Yuan, Y. Liao, L. Mao, J. Zhang, Y. Wang, F. Huang, Y. Jiang, Y. He, W. Ding, Enhanced biocorrosion
531 resistance and biocompatibility of degradable Mg-Nd-Zn-Zr alloy by brushite coating, Mater Sci Eng C Mater Biol Appl
532 33(8) (2013) 4833-41.
533 [57] L. Mao, G. Yuan, J. Niu, Y. Zong, W. Ding, In vitro degradation behavior and biocompatibility of Mg–Nd–Zn–Zr
534 alloy by hydrofluoric acid treatment, Mater. Sci. Eng., C 33(1) (2013) 242-250.
535 [58] B. Trappmann, B.M. Baker, W.J. Polacheck, C.K. Choi, J.A. Burdick, C.S. Chen, Matrix degradability controls
536 multicellularity of 3D cell migration, Nat Commun 8(1) (2017) 371.
537 [59] P.M. Tsimbouri, P.G. Childs, G.D. Pemberton, J. Yang, V. Jayawarna, W. Orapiriyakul, K. Burgess, C. González-
538 García, G. Blackburn, D. Thomas, C. Vallejo-Giraldo, M.J.P. Biggs, A.S.G. Curtis, M. Salmerón-Sánchez, S. Reid, M.J.
539 Dalby, Stimulation of 3D osteogenesis by mesenchymal stem cells using a nanovibrational bioreactor, Nature Biomedical
540 Engineering 1(9) (2017) 758-770.
541

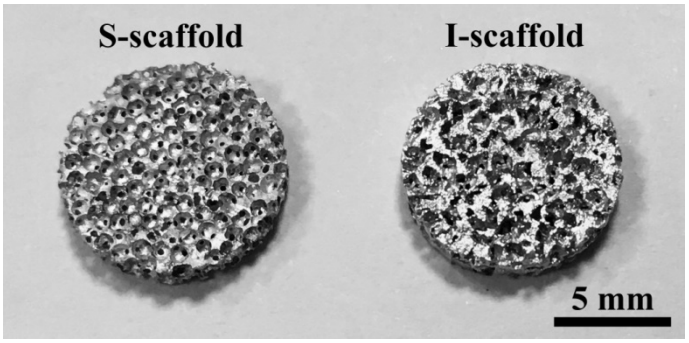

Fig. 1. Optical image of the two Mg scaffolds.

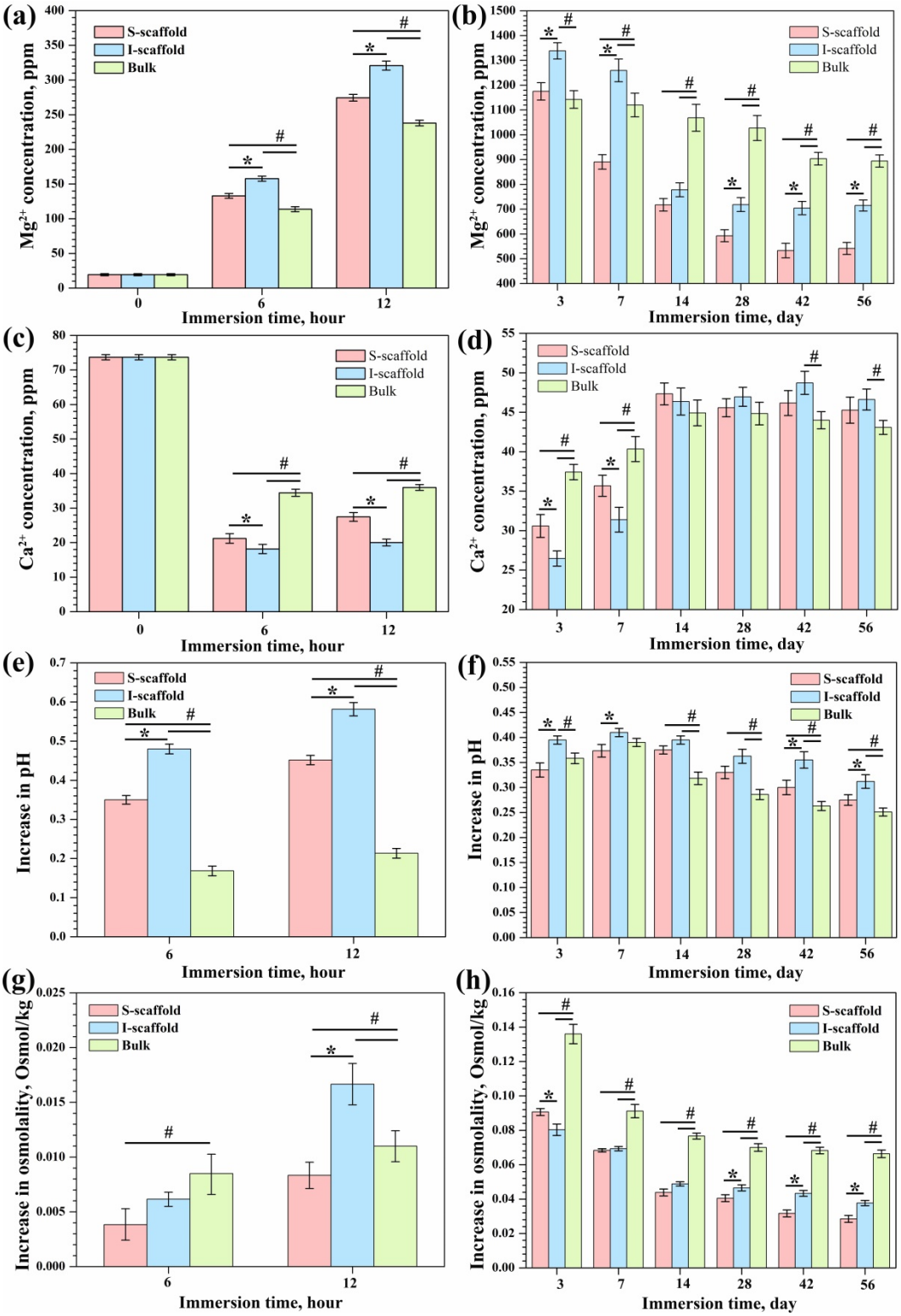

Fig. 2. Mg^{2+} (a, b) and Ca^{2+} (c, d) concentrations of the extracts, increases in pH (e, f) and osmolality (g, h) of the extracts. *Significant difference between S-scaffold and I-scaffold. #Significant difference between scaffold group and bulk group.

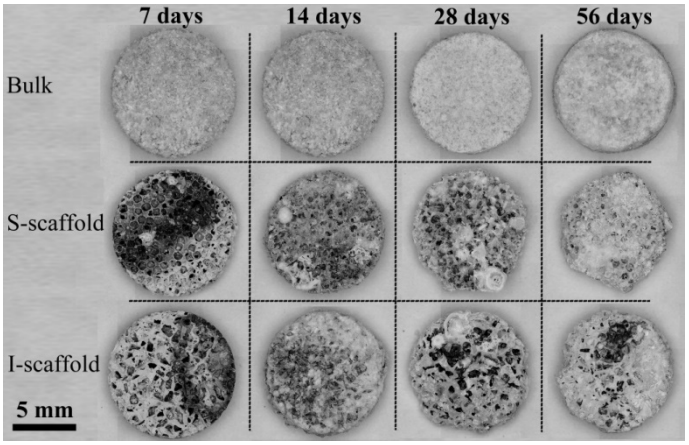

Fig. 3. Macrographs of the representative Mg scaffolds after immersion tests.

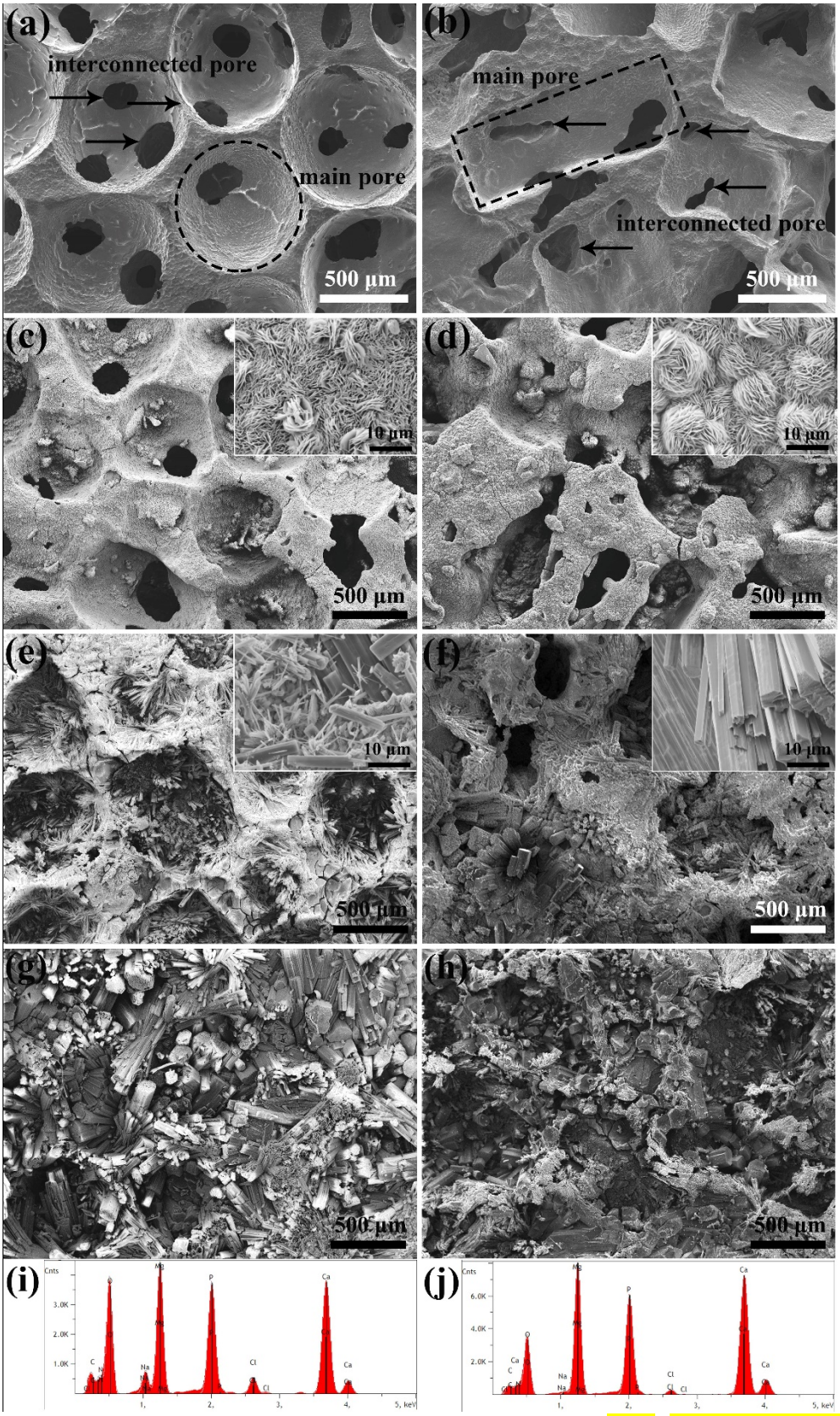

Fig. 4. SEM images of the representative scaffolds after immersion tests; (a) 0 d, (c) 7 d, (e) 14 d and (g) 56 d for S-scaffolds; (b) 0 d, (d) 7 d, (f) 14 d and (h) 56 d for I-scaffolds; (i) and (j) are EDS analysis of degraded S-scaffold and I-scaffold at 14 d; the inserted images are magnified view of degradation products.

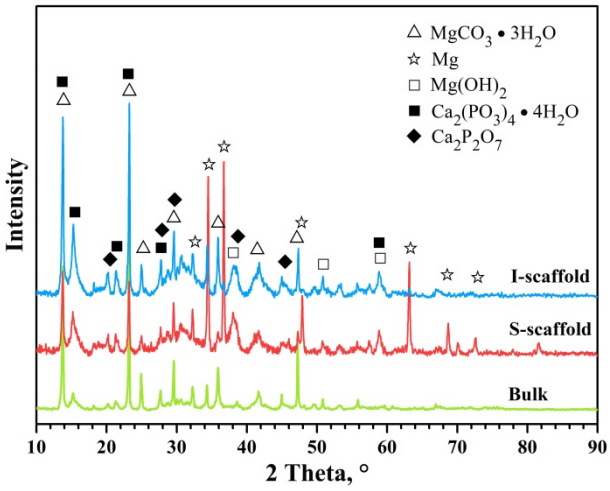

Fig. 5. XRD analysis of the degradation products.

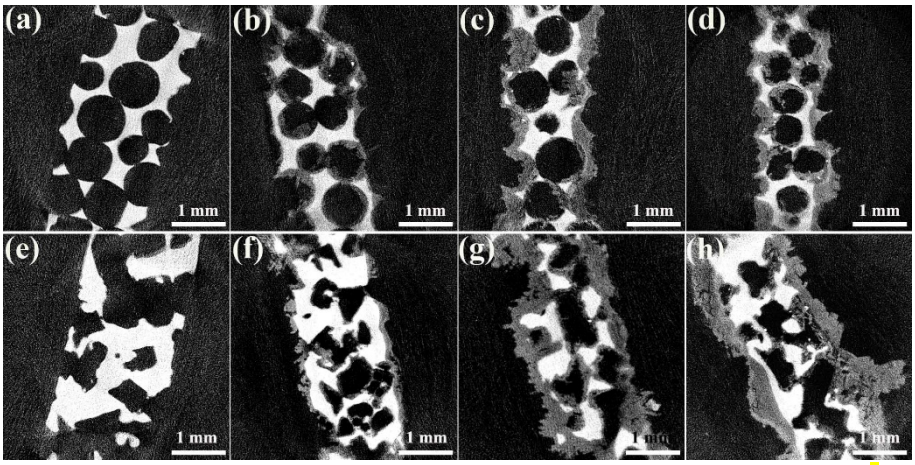

Fig. 6. Micro-CT inspections of the representative scaffolds after immersion tests; (a) 0 d, (b) 14 d, (c) 28 d and (d) 56 d for S-scaffold; (e) 0 d, (f) 14 d, (g) 28 d and (h) 56 d for I-scaffold.

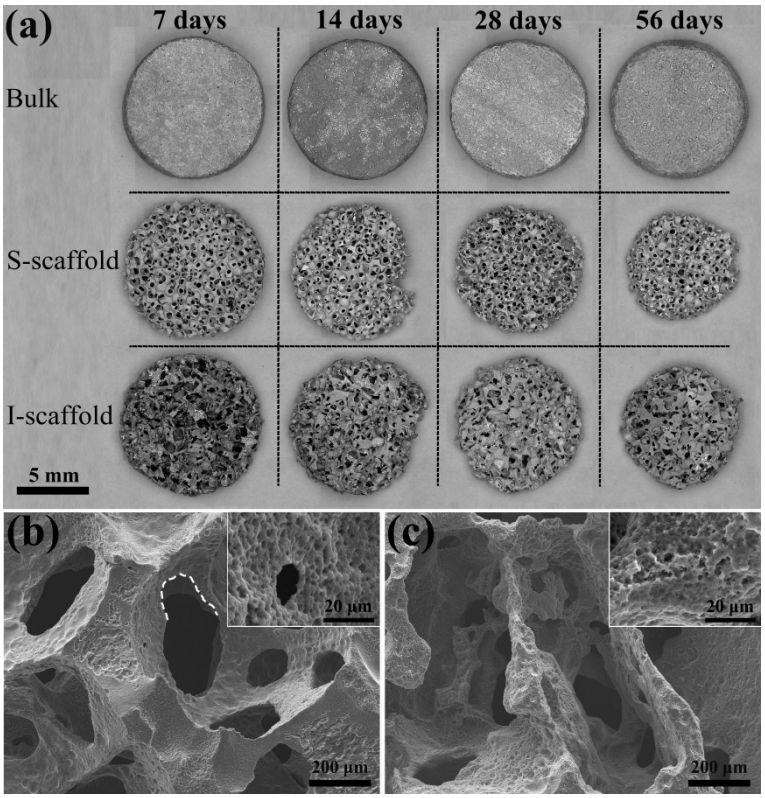

Fig. 7. Macrographs of the representative Mg scaffolds after removal of degradation products (a), SEM image of S-scaffold at 56 d (b), SEM image of I-scaffold at 56 d (c).

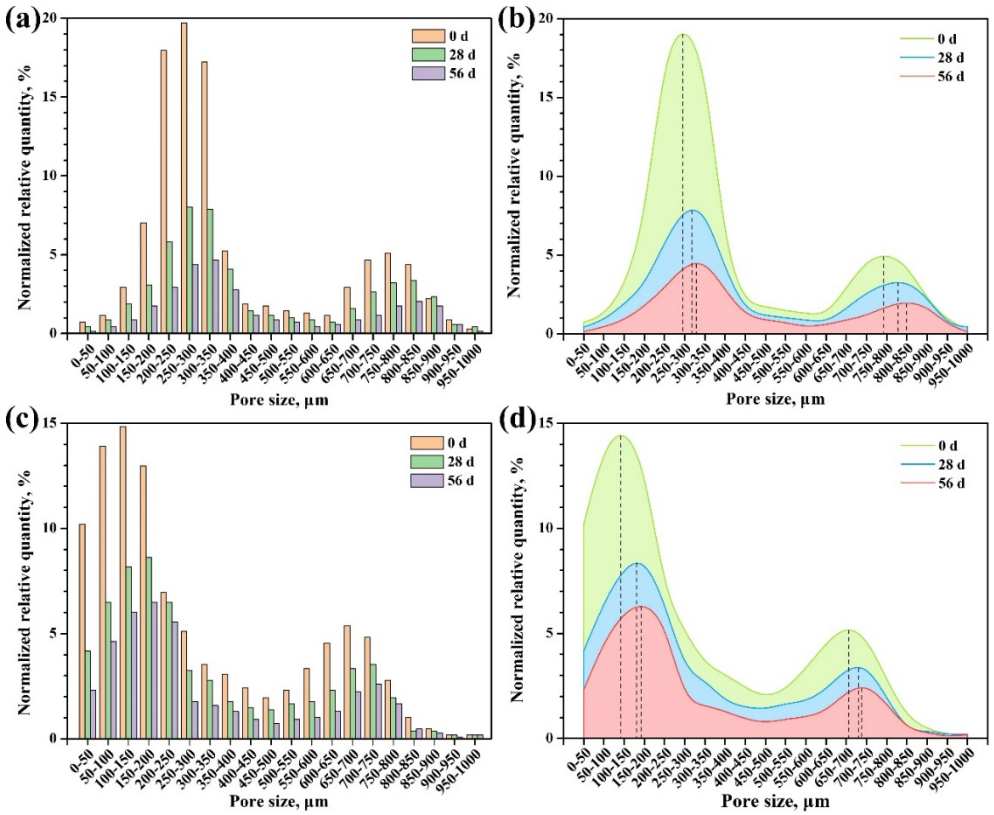

Fig. 8. Pore size distribution of the degraded S-scaffold (a, b) and I-scaffold (c, d).

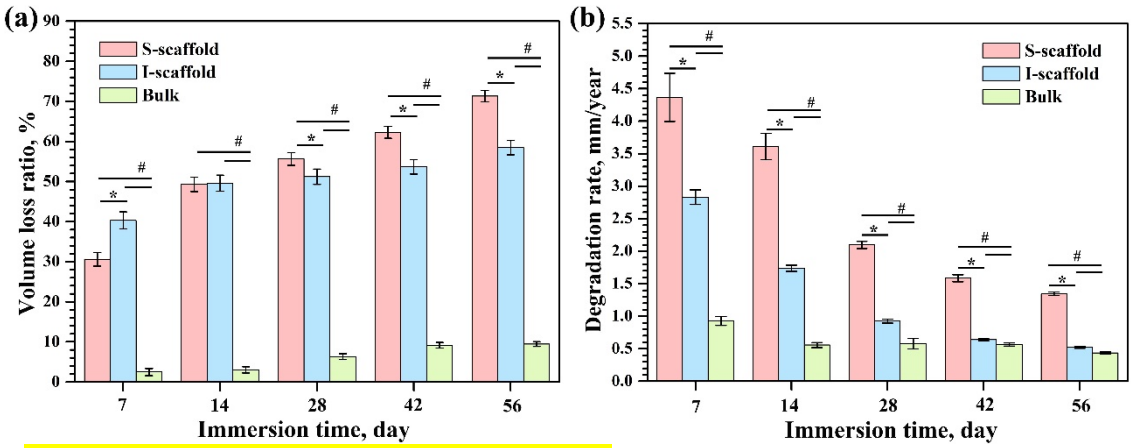

Fig. 9. Volume loss ratio (a) and degradation rates (b) of the specimens. *Significant difference between S-scaffold and I-scaffold. #Significant difference between scaffold group and bulk group.

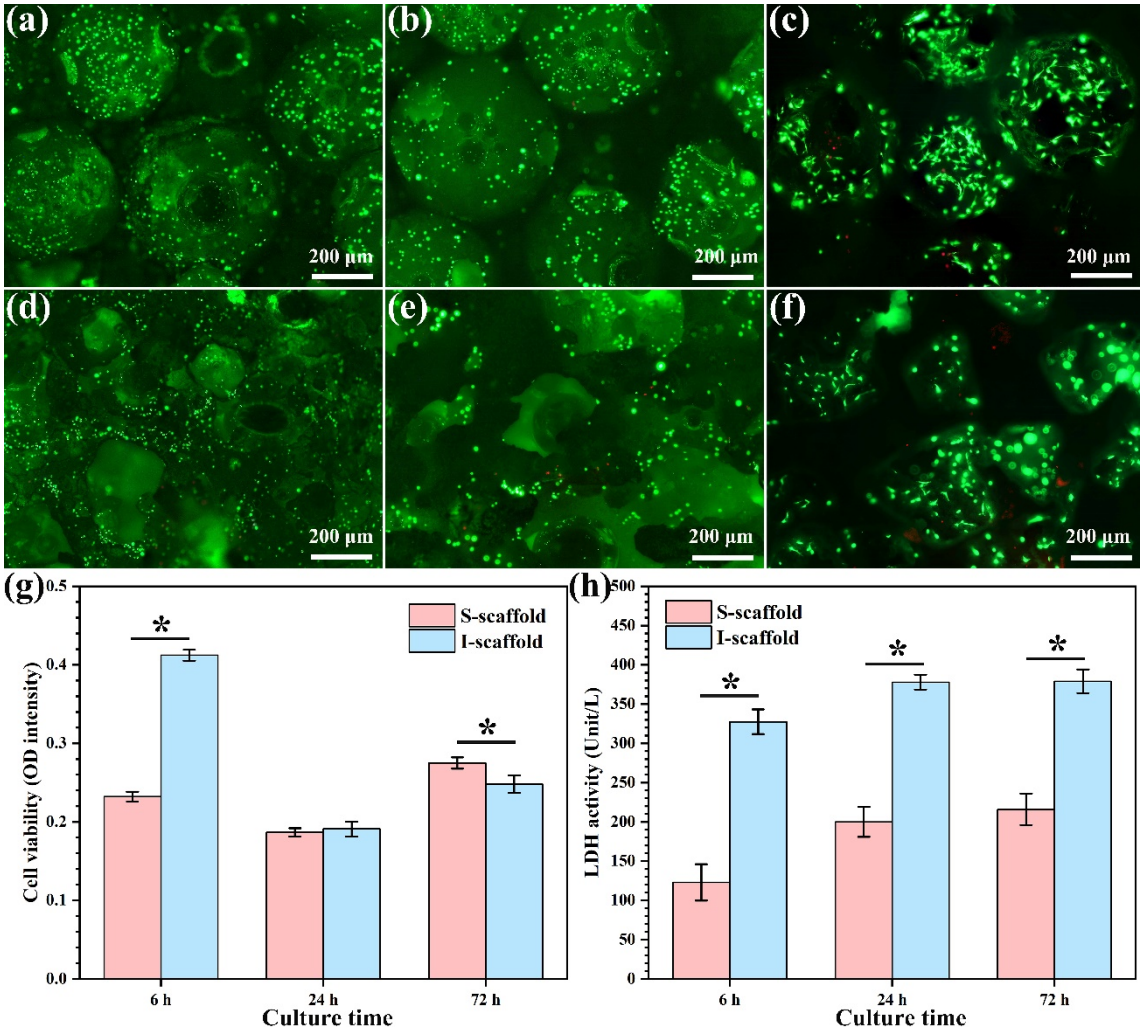

Fig. 10. Cytocompatibility of the two Mg scaffolds: (a) 6 h, (b) 24 h and (c) 72 h for S-scaffold; (d) 0 h, (e) 24 h and (f) 72 h for I-scaffold; (g) cell viability and (h) LDH activity. *Significant difference between S-scaffold and I-scaffold.

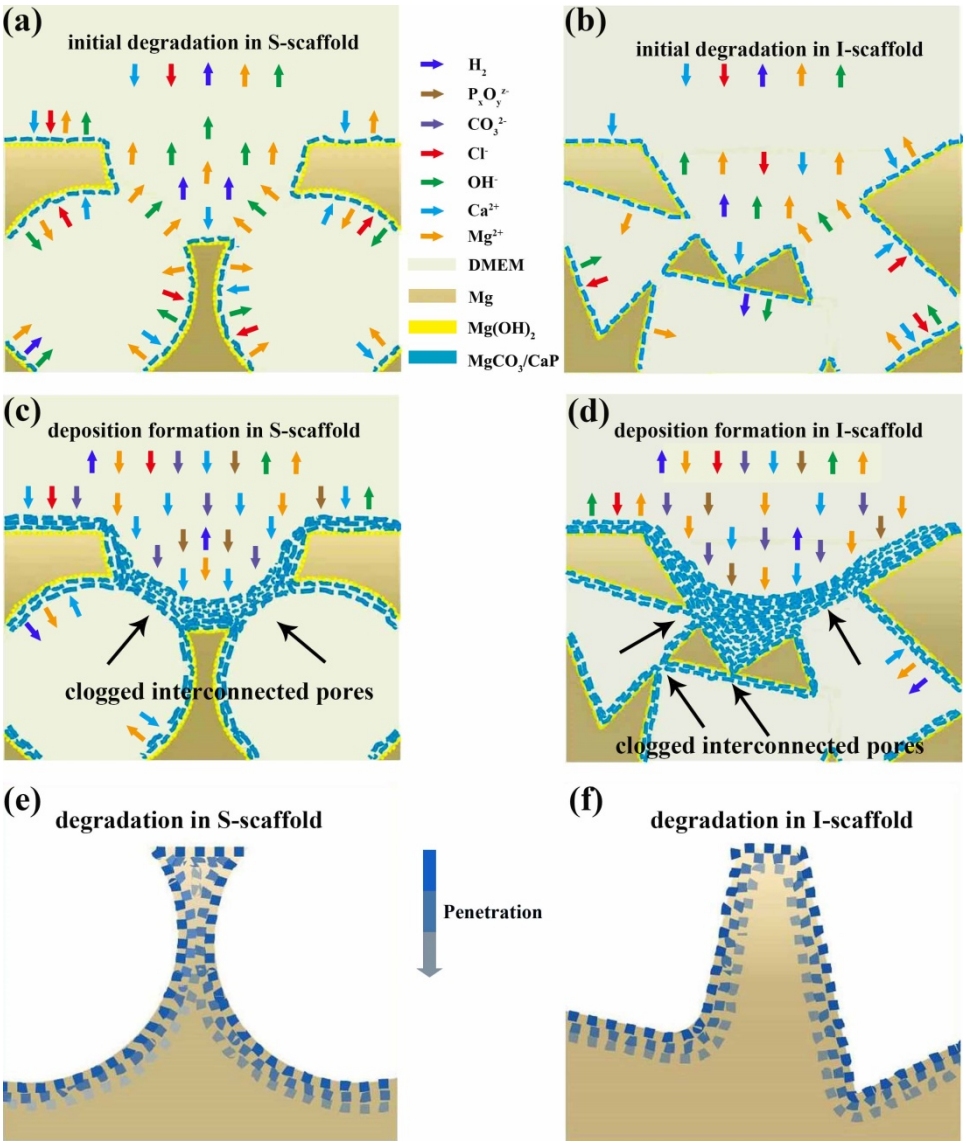

Fig. 11. Schematic illustration of the deposition and the degradation mechanism of the two Mg scaffolds.

Table. 1 Pore characteristics of the two Mg scaffolds.

Specimen	Porosity, %	Main pore size, μm	Interconnected pore size, μm	Surface area/ Object volume, /mm
I-scaffold	68.54±1.22	~ 750	0-400	7.37±0.51
S-scaffold	75.14±0.35	~ 750	150-400	3.43±0.15
Bulk form	-	-	-	1.41±0.01